NAS5-31716

NASA-CR-204994

Satellite-Sensor Calibration Verification Using The Cloud-Shadow Method

by

035147

P. Reinersman, K.L. Carder, and F.R. Chen

Marine Science Department

University of South Florida

St. Petersburg, Florida

Abstract

An atmospheric-correction method which uses cloud-shaded pixels together with pixels in a neighboring region of similar optical properties is described. This cloud-shadow method uses the difference between the total radiance values observed at the sensor for these two regions, thus removing the nearly identical atmospheric radiance contributions to the two signals (e.g. path radiance and Fresnel-reflected skylight). What remains is largely due to solar photons backscattered from beneath the sea to dominate the residual signal. Normalization by the direct solar irradiance reaching the sea surface and correction for some second-order effects provides the remote-sensing reflectance of the ocean at the location of the neighbor region, providing a known "ground target" spectrum for use in testing the calibration of the sensor.

A similar approach may be useful for land targets if horizontal homogeneity of scene reflectance exists about the shadow. Monte Carlo calculations have been used to correct for adjacency effects and to estimate the differences in the skylight reaching the shadowed and neighbor pixels.

Key words: Satellite calibration, cloud shadow.

Introduction

Accurate calibration of aircraft and space-borne sensors that view dark targets such as the ocean is critical. As much as 90% of the signal at the sensor is due typically to the atmosphere; as little as 10% of the signal may be due to target reflectance[1,2]. Therefore, a 5% sensor-calibration error may result in an error of as much as 50% in the calculated reflectance. Prelaunch calibration accuracies of 2-5% are representative of requirements for space sensors, and in-orbit sensor performance typically differs from prelaunch performance. Since sensor performance degrades over the life of the mission, occasional recalibration using aircraft- or ground-based methods[3,4] is required.

The method of choice for sensor calibration when viewing the ocean from aircraft or space is to locate a region with relatively stable and homogeneous optical properties (e.g. the Sargasso Sea), measure its water-leaving radiance spectrum, and determine the optical properties of the atmosphere coincidentally with a sensor overpass[4,2,5]. For coastal applications with variable bottom reflection and horizontal gradients in water constituents, locating a region where surface calibration can be accurately performed is often quite difficult.

In this work we describe an atmospheric-correction method that uses cloud-shadowed pixels in combination with unshadowed pixels in a neighboring region of similar optical properties. The cloud-shadow method uses the difference between water-leaving radiance values $L_w(\lambda)$ for these two regions. This allows nearly identical contributions to the two signals (e.g. path radiance and Fresnel-reflected skylight) to be removed, leaving mostly solar photons backscattered from beneath the sea to dominate the residual signal. Normalization by the direct solar irradiance reaching the sea surface provides, to first order, the remote-sensing reflectance of the ocean at the location of the neighbor region. Special

attention must be paid to evaluating and correcting for adjacency effects and the difference in skylight reaching the shadowed and neighbor pixels.

The Airborne Visible-InfraRed Imaging Spectrometer (AVIRIS), flying at an altitude of 20 km, provides data simulating that expected from hyperspectral space sensors of the future.[6] Data from AVIRIS were used to develop and test the methodology described in this paper.

Theoretical Considerations

For illustrative purposes, imagine a viewing scenario in which the sensor calibration is correct. The solar zenith angle, θ_0, is 45°, and the angle from the pixel to the sensor, θ, is about 0° (see Fig. 1). A small, compact cumulus cloud removes direct solar photons and shadows a region. The water-leaving radiance directed toward the sensor from this shadowed region is designated L_{ws}. (Note that terms indicating wavelength-dependence have been left out for brevity in cases where doing so is unlikely to cause confusion.) This radiance results from skylight photons reflected by the surface or scattered from beneath the ocean surface.

Adjacent to the shadowed region is a neighboring patch of water with inherent optical properties identical to those of the shadowed region. This region is illuminated by direct, solar photons as well as skylight . The water-leaving radiance from the neighbor region is designated L_{wn}.

In addition to the water-leaving radiance, the sensor measurement includes the effects of path radiance caused by atmospheric scattering of photons into the field of view of the sensor. The primary processes responsible for path radiance are molecular, or Rayleigh, scattering, and particulate, or aerosol scattering. Path radiance may be attributed, therefore, to photons which have suffered only Rayleigh scattering, only aerosol scattering, or some

combination of both. These three types of path radiance are denoted by L_r, L_a, and L_{ra}, respectively.

Accordingly, let the total radiance measured at the sensor when viewing a neighboring area in unshadowed water be given by

$$L_{tn} = L_r + L_a + L_{ra} + t_d L_{wn} \quad , \qquad (1)$$

where t_d represents the diffuse transmittance of the atmosphere for water-leaving radiance[7].

The radiance measured at the sensor when viewing a shadowed pixel may be expressed in the same form, but some differences in the path radiances and diffuse transmittance may be expected. We assume that the cloud is of sufficient thickness that the direct solar beam is completely occluded. Since part of the viewing path to the shadowed pixel is also shadowed, this portion of the viewing path must produce less path radiance (Fig. 1).

The apparent path transmittance of the water-leaving radiance from the shadowed pixel may not be equivalent to the term used in Eq. (1). Use of the "diffuse transmittance" is justified when viewing a large, homogeneous area. In such a case, target radiance scattered out of the viewing path is balanced by the radiance scattered into it from adjacent areas of the scene. In the case of the shadowed pixel, the adjacent areas of the scene are generally brighter, and so the apparent transmittance of the viewing path to the shadow will be enhanced by photons emanating from the bright portion of the image and scattered into the field of view of the sensor.

With these ideas in mind, the total radiance at the sensor when viewing a shadowed pixel may be written

$$L_{ts} = L_r - \Delta L_r + L_a - \Delta L_a + L_{ra} - \Delta L_{ra} + (t_d + \Delta t_d) L_{ws} \quad , \qquad (2)$$

where Δ terms express perturbations due to nonhomogeneity in the scene illumination.

In general, water-leaving radiance is the result of backscattering of light which has penetrated the air-sea interface, and may be expressed as the sum of two parts: one part caused by backscattering of diffuse skylight, and the other by backscattering of the direct solar beam. For the neighbor and shadowed pixels, respectively,

$$L_{wn} = {}_{sky}L_{wn} + {}_{sol}L_{wn} \quad , \qquad L_{ws} = {}_{sky}L_{ws} \quad , \tag{3}$$

since ${}_{sol}L_{ws} = 0$.

Even though the cloud is small and occludes a similar portion of the sky for both the shadowed and neighbor pixels, the diffuse irradiances incident on the two pixels are unequal (see appendix). The cloud occludes the brightest part of the sky from the shadowed pixel, i.e. the part containing the radiance due to near-forward scattering by aerosols. On the other hand, the neighbor pixel is illuminated by the relatively bright side of the cloud. Therefore, the diffuse irradiance at the neighbor pixel may be greater than that in the shadow. Under the assumption that the remote sensing reflectance for skylight is about the same at the shadow and neighbor pixels, we may write

$${}_{sky}L_{wn} = {}_{sky}L_{ws} + {}_{\Delta sky}L_{ws} \quad , \tag{4}$$

so that

$$L_{tn} - L_{ts} = \Delta L_r + \Delta L_a + \Delta L_{ra} + t_d\,({}_{sol}L_{wn} + {}_{\Delta sky}L_{ws}) - \Delta t_d\ {}_{sky}L_{ws} \quad . \tag{5}$$

The first three terms on the right of Eq. (5) depend on the length of the shaded portion of the viewing path to the shadow pixels. The height of the intersection of the viewing path and the upper edge of the cylinder of atmosphere shaded by the cloud can be determined from scene geometry. The layer of atmosphere below this intersection would be the source of less than 15% of the Rayleigh scattering, so we will assume that the

Rayleigh-aerosol correction term, ΔL_{ra}, is negligible. Then, following Gordon et al.[8], for the aerosol and Rayleigh corrections we may write

$$\Delta L_x = \{ \omega_x \tau'_x F''_0 P_x(\theta, \theta_0) \} t'_d / 4\pi \quad , \qquad x = a , r , \qquad (6)$$

where

τ'_x = optical thickness of shaded viewing path for process x;

ω_x = single-scattering albedo for process x;

F_0'' = $F_0 \exp(-(\tau - \tau')/\cos(\theta_0))$, direct beam incident at height of shadow/path intersection;

F_0 = extra-terrestrial solar irradiance;

$P_x(\theta,\theta_0)$ = $\{ P_x(\theta_-) + [\rho(\theta) + \rho(\theta_0)] P_x(\theta_+) \} / \cos(\theta)$;

$\cos(\theta_{+-})$ = $+-\cos(\theta_0)\cos(\theta) + \sin(\theta_0)\sin(\theta)\cos(\phi-\phi_0)$;

$\rho(\theta)$ = Fresnel reflectance for incident angle θ;

$P_x(\theta)$ = scattering phase function for process x;

t'_d = $\exp\{-((\tau_r - \tau'_r)/2 + (\tau_{oz} - \tau'_{oz}))/\cos(\theta) \}$, diffuse transmittance from shadow/path intersection to top of atmosphere.

A term involving $(\tau_a - \tau'_a)$ and was neglected in the last expression because diffuse transmissivity due to aerosols from the top of this layer is approximately unity[2]. Also, since ozone is generally found above the cloud layer, the term τ'_{oz} is also negligible.

The term involving Δt_d in Eq. (2) represents the apparent increase in diffuse transmittance of water-leaving radiance when viewing a shadowed pixel. The work of

Tanre et al.[9] indicates that this term is proportional to the difference in water-leaving radiances from the shadowed and neighbor pixels, and is dependent on the geometry of the particular case. We will express Δt_d as

$$\Delta t_d = t_d \, \sigma \, (L_{wn} - L_{ws}) / L_{ws} = t_d \, \sigma \, ({}_{sol}L_{wn} + {}_{\Delta sky}L_{ws}) / {}_{sky}L_{ws} . \quad (7)$$

Unlike for the $\Delta L_x(\lambda)$ terms, the values for σ, and hence $\Delta t_x(\lambda)$, can not be determined using Lowtran 7[10]. For this application, σ was estimated using approximations developed in Reinersman et al.[11] (Fig. 2). These approximations are based on linear scaling of Elterman's[12] atmosphere to match the prevailing atmospheric aerosol optical thickness. To get an initial estimate of $\tau_a(\lambda)$, a scaling relationship between L_a(780 nm) and the aerosol optical thickness, τ_a(780 nm), was developed using Lowtran 7 (Fig. 3). First, L_t(780 nm) was calculated for several values of τ_a(780 nm). Then L_t(780 nm) was calculated for an atmosphere characterized by Rayleigh scattering only. Subtraction of the latter value from the L_t(780 nm) values calculated for the atmospheres containing aerosols yields L_a(780 nm) because $L_r(\lambda) + L_{ra}(\lambda)$ is approximately constant for $\tau_a(\lambda) < .5$. Based on the above simulations, we estimate that σ(550 nm) is about 0.06 for shadows of spherical clouds of the size modelled in this paper when viewed through very clear atmospheres (τ_a(550 nm) = .0375).

Using Eqs. (7) and (5) we obtain

$$({}_{sol}L_{wn} + {}_{\Delta sky}L_{ws}) = \{ L_{tn} - L_{ts} - \Delta L_a - \Delta L_r \} / t_d(1 - \sigma) . \quad (8)$$

Now define[8]

$$\varepsilon(\lambda_i,\lambda_j) = \{ \omega_a(\lambda_i) \tau'_a(\lambda_i) P_a(\theta,\theta_0,\lambda_i) \} / \{ \omega_a(\lambda_j) \tau'_a(\lambda_j) P_a(\theta,\theta_0,\lambda_j) \} , \quad (9)$$

and

$$S'(\lambda_i, \lambda_j) = \Delta L_a(\lambda_i) / \Delta L_a(\lambda_j) = \varepsilon(\lambda_i, \lambda_j) \{ F''_0(\lambda_i) t'_d(\lambda_i) \} / \{ F''_0(\lambda_j) t'_d(\lambda_j) \}. \quad (10)$$

Using these results in Eq. (8)

$$t_d(\lambda_i)(1 - \sigma(\lambda_i))\{ {}_{sol}L_{wn}(\lambda_i) + {}_{\Delta sky}L_{ws}(\lambda_i) \} = L_{tn}(\lambda_i) - L_{ts}(\lambda_i) - \Delta L_r(\lambda_i)$$

$$-S'(\lambda_i, \lambda_j)\{ L_{tn}(\lambda_j) - L_{ts}(\lambda_j) - \Delta L_r(\lambda_j) - t_d(\lambda_i)(1 - \sigma(\lambda_i))({}_{sol}L_{wn}(\lambda_j) + {}_{\Delta sky}L_{ws}(\lambda_j)) \} \quad . \tag{11}$$

If λ_j is a wavelength such as 780 nm where the water-leaving radiance is essentially zero, then ${}_{sol}L_{wn}(\lambda_j) + {}_{\Delta sky}L_{ws}(\lambda_j) = 0$, and Eq. (5) becomes

$$\Delta L_a(780 \text{ nm}) = L_{tn}(780 \text{ nm}) - L_{ts}(780 \text{ nm}) - \Delta L_r(780 \text{ nm}) . \tag{12}$$

This allows Eq. (11) to be written

$$t_d(\lambda_i)(1 - \sigma(\lambda_i))\{ {}_{sol}L_{wn}(\lambda_i) + {}_{\Delta sky}L_{ws}(\lambda_i) \} = L_{tn}(\lambda_i) - L_{ts}(\lambda_i) - \Delta L_r(\lambda_i)$$

$$-S'(\lambda_i, 780 \text{ nm})\{ L_{tn}(780 \text{ nm}) - L_{ts}(780 \text{ nm}) - \Delta L_r(780 \text{ nm}) \} \quad . \tag{13}$$

From scene geometry, the cloud height, h, and height of the shadowed viewing path can be calculated. Then, $\Delta L_r(\lambda)$ can be determined for all λ by subtracting Lowtran 7 results for the air column down to height h from the results for the entire air column. The aerosol correction term, $\Delta L_a(780 \text{ nm})$, is then determined by Eq. (12). Knowledge of wind speed allows estimation of $\varepsilon(\lambda_i, 780 \text{ nm})$[13], and thus $S'(\lambda_i, 780 \text{ nm})$. ${}_{\Delta sky}L_{ws}(\lambda_i)$ may be estimated by Monte Carlo simulation (see appendix). Thus, Eq. (13) allows ${}_{sol}L_{wn}(\lambda_i)$ to be calculated.

If we assume a Lambertian sky, the average cosine for irradiance at the surface due to skylight, ${}_{sky}E_d(0^+)$, is 0.707[14]. This is roughly equivalent to having all skylight photons striking the sea surface at 45°, and is the same as the cosine of the irradiance due to direct solar illumination, ${}_{sol}E_d(0^+)$, in this example. So, since reflectance is independent of the

source intensity and color, and illumination geometry is equivalent for the solar and average sky photons,

$$ {}_{sol}R_{rs} = {}_{sol}L_{wn} / {}_{sol}E_d(0^+) = L_w / E_d(0^+) = R_{rs}, \qquad (14) $$

where R_{rs} is the remote-sensing reflectance due to total downwelling irradiance, $E_d(0^+)$. Thus, deriving R_{rs} in this manner provides a calibrated target reflectance value that can be used to derive the atmospheric aerosol characteristics in a manner similar to that used by Gordon et al.[8] for low-chlorophyll, offshore waters.

Experiment

The cloud-shadow reflectance method was tested using Airborne Visible-InfraRed Imaging Spectrometer(AVIRIS) data collected from an altitude of 65,000 ft over the Straits of Florida. AVIRIS produces images consisting of 512 rows of 614 cross-track samples. At each sample location radiance is measured simultaneously in 224 channels. Spatial resolution for nadir viewing is 20 m.

We calibrated the Airborne Visible-InfraRed Imaging Spectrometer(AVIRIS) at a clear-water offshore location in the Florida Current using the vicarious calibration method of Carder et al.[5] In brief, the R_{rs} curves for calibration scenes are measured; the values of $E_d(0^+)$ are obtained from Lowtran 7; and $L_w(\lambda)$ values are calculated by multiplying R_{rs} by $E_d(0^+)$. This technique maintains consistency between the illumination for the atmospheric correction program and the ocean measurements. The extra-terrestrial solar radiance F_0 provided by Neckel and Labs[15] has been used as the solar source for all model calculations. Then Lowtran 7 was used to calculate the total radiance, L_t, reaching the sensor from the ocean and the atmosphere. The resulting data were median-filtered using the brightness at 780 nm to discriminate against some 10% of the pixels apparently containing white caps and/or sun glint. Crests of waves of about 100 m in wavelength were observed in the

imagery, and this enhanced brightness would have been misinterpreted by the program as being part of the atmospheric path radiance. Finally, the calibration of the sensor was adjusted so that modelled and measured L_t values matched. The first test of the cloud-shadow method was verification that the correct $R_{rs}(\lambda) = L_w(\lambda) / E_d(\lambda)$ spectrum could be recovered from data acquired from an improperly calibrated sensor. $L_t(\lambda)$ spectra from the bottom cloud-shadow pair of Fig. 4 (Cloud 1), calibrated as described above, were used to perform the verification. The test procedure was as follows:

1) The "true" $L_t(\lambda)$ spectra from both the shadow and neighbor pixels were increased by 10% to simulate spectra, $L'_t(\lambda)$, which would have been acquired had the sensor calibration been in error by 10%.

2) ${}_{sol}L'_{wn}(\lambda)$ was calculated from Eq. (5) as described earlier using $L'_t(\lambda)$. Then the first estimate of the remote-sensing reflectance spectrum, $R'_{rs}(\lambda)$, was obtained from

$$R'_{rs}(\lambda) = {}_{sol}L'_{wn}(\lambda) / {}_{sol}E_d(\lambda) \qquad (15)$$

3) Corrected $L'_t(\lambda)$ spectra at the aircraft were simulated by adding atmospheric effects derived from Lowtran 7 for the appropriate conditions, i.e. , a nadir-viewing sensor, a 50.8° sun angle, a 60 km visibility through a marine aerosol with 80% relative humidity and 1014 mb atmospheric pressure.

The iteration process consisted of repeating steps 2 and 3 above. The results of this method are shown in Fig. 5. Both the "true" and "miscalibrated" reflectance spectra are illustrated along with the intermediate results from the cloud-shadow method. After four iterations of recalibration, the "corrected" cloud shadow reflectance spectrum approximates the "correct" spectrum as closely as if the correct calibration had been used initially.

The method is effective for two reasons: 1) the error in the solar spectrum used to illuminate the atmosphere in the Lowtran 7 calculations is less than 2%; 2) the atmospheric

effects simulated by Lowtran 7 account for most of the radiance L_t measured by the sensor, and for clear days this can be very accurately determined. If the sensor calibration were 10% too large, the L_w spectrum calculated conventionally from the difference between L_t and $(L_a + L_r)$ would contain nearly all of the error. Thus, the conventionally calculated L_w could be 40% or more higher than the true curve. The atmospheric path radiance removed inherently by the cloud-shadow method leaves an estimated L_w spectrum that is high by only about 10%, however. Since this spectrum is closer to the correct one, recalibration based upon this new ground-target reflectance provides a better basis for a second iteration of the recalibration loop, providing a calibration factor that is in error by less than 5%. With iteration, convergence toward a calibration factor consistent with the solar spectrum and the model atmosphere used in Lowtran 7 is assured.

Results and Discussion

Two further demonstrations of the cloud-shadow atmospheric-correction method were performed using the scene shown in Fig. 4. The data were collected on a SE-NW transect from the Florida Current to Biscayne Bay. Elliot Key is shown in the upper left corner offshore. The shadow-neighbor pairs are near the seaward reef edge of Biscayne National Park. The cloud image associated with the bottom pair (Cloud 1) is recorded on the adjoining scene. Moments before this imagery was collected, AVIRIS acquired data for calibration over the Florida Current from a scene some 25 km to the southeast.

The results of applying the cloud-shadow method to Cloud 1 are compared to conventionally derived results in Fig. 6. Results shown for the conventional method were derived as described in Carder et al.[5] with one exception: the water-leaving radiance at 780 nm could not be assumed to be zero, as the method usually requires, because of sunglint and/or foam effects due to the 10-12 m/s winds[16]. Instead, the water-leaving radiance at 780 nm was assumed to equal that determined by the cloud-shadow method, since it

inherently separates the atmospheric radiance from all water-leaving radiance including sunglint and foam effects. The reflectance derived using the cloud shadow method differs from the conventional result by less than 10% from 400 nm to about 460 nm. From 460 nm up to 900 nm agreement is within 5% except for a minor perturbation at about 765 nm.

The results of applying the method to the top shadow-neighbor pair (Cloud 2) are illustrated in Fig. 7. For this region the cloud-shadow reflectance spectrum is as much as 15% below that for the conventional approach for wavelengths less than 580 nm. For longer wavelengths the comparison is still excellent. The area about the shadow of Cloud 2 appears less isotropic than that about the shadow of Cloud 1, perhaps contributing to the larger difference. The conventional method, however, would have seriously over-corrected for aerosol radiance had sunglint and/or foam effects not been detected and separated out using the cloud-shadow method.

Thus, although the cloud-shadow method cannot provide a correction for the entire image (unless the aerosol concentration and type are horizontally homogeneous), it can be used effectively to provide an independent check for specific locations to help identify problems resulting from sensor calibration or atmospheric-removal methodology.

Appendix

The term ${}_{\Delta sky}L_{ws}$ (= ${}_{sky}L_{wn}$ - ${}_{sky}L_{ws}$) which appears in Eq. (13) cannot be derived from Lowtran 7. Instead, this quantity was estimated using backward Monte Carlo simulation[11, 17, 18]. The modelled atmosphere consisted of 50 horizontally infinite and homogeneous layers overlying a flat sea surface. Optical properties of the atmosphere were taken from Elterman[12], with Rayleigh and marine aerosol phase functions as in Reinersman and Carder[11].

The quantites of interest in these calculations were the differences in downward diffuse irradiances needed to calculate $_{\Delta sky}L_{ws}$. Photons reflected from the surface of the sea make some contribution to $E_d(0^+)$, as do photons backscattered back into the atmosphere from below the sea surface. But these contributions to $E_d(0^+)$ are probably about the same in the shadow and neighbor regions, and would cancel each other in the calculation of $_{\Delta sky}L_{ws}$. So, for simplicity, the sea surface was modelled as a perfect absorber, and photons which would have impinged upon the sea surface more than once were neglected.

Clouds were modelled as spheres which completely displaced the atmosphere in which they were imbedded. The extinction coefficient within clouds was set at 50 km^{-1}, and the single scattering albedo was set to unity[19]. Scattering within clouds was governed by a single-term Henyey-Greenstein phase function with the asymmetry factor set to .85.[20] In the results to follow, Cloud 1 and Cloud 2 represent the bottom and top cloud-shadow pairs of Fig. 4, respectively. Cloud 1 has a radius of 372 m and a center height of 942 m. Cloud 2 has a radius of 350 m and a center height of 1194 m. These parameters were based on estimation of the areas of the shadows and the solar zenith angle of 50.8°.

Photon packets were traced backward from a receiver located on the surface at a point of interest using a method derived from Gordon[18]. Each simulation in this work traced 10^5 packets, each initially representing 10^{10} photons, until the weight of the packet was diminished to less than 1 photon. Estimates of the downward diffuse irradiance (normalized by the extraterrestrial solar irradiance) and the average cosine of the downward diffuse irradiance were acquired for each sensor position modelled.

Preliminary simulations indicated that the diffuse light field is highly variable in the region near and within the shadow. Figs. 8 and 9 show the normalized diffuse irradiance and the average cosine for diffuse irradiance at the surface in the vicinity of model Cloud 1.

These plots represent results modelled at 400 nm with Elterman's standard atmosphere. The points in Fig. 8 are located in the vertical plane containing the sun, cloud center, and shadow center (SCS plane). The points in Fig. 9 lie on the line perpendicular to the SCS plane through the center of the shadow. Reference lines are included which show the normalized downward diffuse irradiance and average cosine for the same solar zenith angle and atmospheric conditions with no cloud present.

An interesting feature of Fig. 8 is the bright spot appearing directly below and sunward of the cloud. This may be the result of modelling a spherical cloud, since, in this case, part of the brightly illuminated side of the cloud is visible from directly below. The features relevant to this work, however, are the depletion of diffuse irradiance at the center of the shadow, and the distance to which perturbations due to the presence of the cloud extend from the center of the shadow. Many combinations of cloud sizes, cloud heights, and aerosol optical thicknesses were modelled, and the same general features appeared in each case.

Selection of the neighboring region for a cloud shadow involves a compromise. The neighboring region should be near enough to the shadow that the inherent optical properties of the water in both regions are the same, but the neighboring region should be in a location where the downward radiance distribution at the surface is not perturbed by the presence of the cloud. Consider the two half-planes defined by the line through the shadow center and perpendicular to the SCS plane. The results shown in Figs. 8 and 9 indicate that the neighbor region should be located in the half-plane which lies further from the cloud, i.e. on the side of the shadow from which the illuminated face of the cloud is not visible. Neighbor points chosen directly on the SCS plane should be at least 5 cloud radii from the shadow center. Those chosen along the line perpendicular to the SCS plane may be as near as 3 cloud radii to the shadow center.

The data comprising Fig. 10 resulted from modelling Cloud 1 and Cloud 2 under the same conditions just described. The neighbor region was located in each case 3 cloud radii from the shadow center on the line through the shadow center and perpendicular to the SCS plane. The average cosine of the diffuse irradiance at the neighbor regions is indistinguishable from the clear sky (no cloud present) value. The average cosine at the shadow centers varies from the clear sky values by less than 10% in the worst case. The normalized downward diffuse irradiance at the neighbor points is also indistinguishable from the clear sky value. The normalized downward diffuse irradiance at the shadow centers differs between Cloud 1 and Cloud 2 due to differences in cloud sizes and heights.

Elterman's standard atmosphere represents conditions which are much more turbid than those prevailing when the image of Fig. 4 was acquired. Accurate modelling of these very clear conditions required scaling of Elterman's aerosol profile so that $\tau_a(550\ \text{nm}) = .0375$. The simulations for Fig. 10 were repeated using the scaled atmosphere, and the results are shown in Fig. 11. Note that for the clear conditions, the difference in diffuse irradiance at the center of the shadows for the two clouds is negligible, and that the difference in diffuse irradiance between the shadow and neighbor regions is much less than for the turbid conditions shown in Fig. 10.

Geometric arguments dictate that if the average cosines for downward diffuse irradiance were the same in the shadow and neighbor regions, then the remote sensing reflectances for downward diffuse irradiance in the two regions would also be equal. Figures 10 and 11 show that the average cosines are not equal, but vary by less that 10%. For the present, assume that the small differences in downward average cosines may be neglected. Then

$$ {}_{sky}R_{rs(shadow)} = {}_{sky}R_{rs(neighbor)} = R_{rs}\,, \tag{16} $$

and

$$ {}_{\Delta sky}L_{ws} = R_{rs} \left({}_{sky}E_d(0^+)_{(neighbor)} - E_d(0^+)_{(shadow)} \right). \quad (17) $$

The consequences of miscalculating ${}_{\Delta sky}L_{ws}$ can be understood qualitatively by examining its importance in Eq. (13) with respect to the term $({}_{sol}L_{wn} + {}_{\Delta sky}L_{ws})$. Again assuming that Eq. (16) holds

$$ {}_{\Delta sky}L_{ws} / ({}_{sol}L_{wn} + {}_{\Delta sky}L_{ws}) = ({}_{sky}E_d(0^+)_{(neighbor)} - E_d(0^+)_{(shadow)}) $$

$$ / ({}_{sol}E_d(0^+)_{(neighbor)} + {}_{sky}E_d(0^+)_{(neighbor)} - E_d(0^+)_{(shadow)}). \quad (18) $$

The values of the right-hand-side of Eq. (18) are shown in Fig. 12 for Cloud 1 and Cloud 2, each embedded in both Elterman's standard and scaled atmosphere. Note that omission of ${}_{\Delta sky}L_{ws}$ can lead to an error of up to 25% in the calculation of ${}_{sol}L_{wn}$, and hence in R_{rs}, when modelling clouds about the size and height used in this demonstration if they are embedded in a very turbid atmosphere. However, accurate estimation of ${}_{\Delta sky}L_{ws}$ becomes less important when using the cloud-shadow method in very clear conditions, where it contributes less than 3% in the calculation of R_{rs}(700 nm).

Acknowledgments

This work was supported by the National Aeronautics and Space Administration through GSFC Contract NAS5-31716, and by the office of Naval Research through Grant N00014-89-J-1091 to the University of South Florida.

References

1. H.R. Gordon and D.K. Clark, "Clear water radiances for atmospheric correction of coastal zone color scanner imagery," Appl. Opt. **20**, 4175-4180 (1981).

2. H.R. Gordon, "Calibration requirements and methodology for remote sensors viewing the oceans in the visible," Remote Sens. Environ. **22**, 103-126 (1987).

3. W.A. Hovis., J.S. Knoll, and G.R. Smith, "Aircraft measurements for calibration of an orbiting spacecraft sensor," Appl. Opt. **24**, 407-410 (1985).

4. H.R. Gordon and A.Y. Morel, *Remote Assessment of Ocean Color for Interpretation of Satellite Visible Imagery: A Review,* Springer-Verlag, New York, , 1983, 114 pp.

5. K.L. Carder, P. Reinersman, R.G. Steward, R.F. Chen, F. Muller-Karger, C.O. Davis, and M. Hamilton, "AVIRIS calibration and application in coastal oceanic environments," Remote Sens. Environ. **44**, 205-216 (1993).

6. R.O. Green, T.G. Chrien, P.J. Nielson, C.M. Sarture, B.T. Eng, C. Chovit, A.T. Murray, M.L.Eastwood, and H.I. Novack, "Airborne visible/infrared imaging spectrometer (AVIRIS):recent improvements to the sensor and data facility," SPIE Proc., 1937, 180-190, Orlando, 1993.

7. M. Wang and H.R. Gordon, "Atmospheric correction of second generation ocean color sensors: a preliminary algorithm," Appl. Opt. **31**, 4247-4260 (1992).

8. H. R. Gordon, D.K. Clark, J.W. Brown, O.B. Brown, R.H. Evans, and W.W. Broenkow, "Phytoplankton pigment concentrations in the Middle Atlantic Bight: comparison of ship determinations and CZCS estimates," Appl. Opt. **22**, 20-36 (1983).

9. D. Tanre, M. Herman, and P. Dechamps, "Influence of the background contribution upon space measurements of ground reflectance," Appl. Opt. **20**, 3676-3684 (1981).

10. F. Kneizys, E. Shettle, L. Abreu, J. Chetwynd, G. Anderson, W. Gallery, J. Selby, and S. Clough, "User's guide to LOWTRAN-7," Rep. AFGL-TR-88-0177 (U.S. Air Force Geophysics Laboratory, Hanscom Air Force Base, Mass., 1988).

11. Reinersman and K. L. Carder, "Monte Carlo simulation of the atmospheric point-spread function with an application to correction for the adjacency effect," Appl. Opt. **34**, 4453-4471 (1995).

12. L. Elterman, "UV, visible, and IR attenuation for altitudes to 50 km," Report AFCRL-68-0153, (Air Force Cambridge Res. Lab, Bedford, MA, 1968).

13. W. Gregg and K. Carder, "A simple spectral solar irradiance model for cloudless maritime atmosphere," Limnol. Oceanogr. **35**, 1657-1675 (1990).

14. S. Sathyendranath and T. Platt, "The spectral irradiance field at the surface and in the interior of the ocean: A model for applications in oceanography and remote sensing," J. Geophys. Res. **93**, 9270-9280 (1988).

15. H. Neckel and D. Labs, "The solar radiation between 3300 and 12500 A.," Solar Phys. **90**, 205-258 (1984).

16. C. Cox and W. Munk, "Measurements of the Roughness of the sea surface from photographs of the sun's glitter," J. Opt. Soc. of Am. **44**, 838-850 (1954).

17. C. Mobley, B. Gentili, H.R. Gordon, Z. Jin, G.W. Kattawar, A. Morel, T. G. Floppini, K. Stamnes, and R.H. Stavn, "Comparison of numerical models for computing underwater light fields," Appl. Opt. **32,** 7484-7504 (1993)

18. H. R. Gordon, "Ship perturbation of irradiance measurements at sea. 1: Monte Carlo simulations," Appl. Opt. **24**, 4172-4182 (1985).

19. J. Li, D. J. W. Geldart, and Petr Chylek, "Solar radiative transfer in clouds with vertical internal inhomogeneity," J. Atmos. Sci., **51**, 2542-2552 (1994)

20. H. W. Barker, "Solar radiative transfer for wind-sheared cumulus cloud fields," J. Atmos. Sci., **51**, 1141-1156 (1994)

Figure Captions:

Fig. 1: A geometric demonstration scene of a paired cloud and shadow arrangement.

Fig. 2: $\sigma(r,\lambda)$, from backward Monte Carlo simulation.

Fig. 3: A scaling relationship between L_a(780 nm) and τ_a(780 nm) derived from LOWTRAN-7.

Fig. 4: The locations of sites where cloud-shadow method was used. Shadow and neighbor regions are marked by boxes.

Fig. 5: Illustration of the convergence of the cloud-shadow calibration. Solid line is "true" R_{rs}, dotted line is R'_{rs} which would be derived if sensor calibration had been in error by 10%. Intermediate lines indicated the iterative convergence of the cloud-shadow method.

Fig. 6: Remote-sensing reflectance spectra from the bottom site neighborhood of Figure 2 using conventional atmospheric-correction methods and the cloud-shadow method.

Fig. 7: Remote-sensing reflectance spectra from the top site neighborhood of Figure 2 using conventional atmospheric-correction methods and the cloud-shadow method.

Fig. 8: Normalized downward diffuse irradiance and average cosine for diffuse irradiance in the vicinity of Cloud 1 at 400 nm in Elterman's standard atmosphere. Points lie on the surface in the vertical plane containing the sun, cloud, and shadow center.

Fig. 9: Normalized downward diffuse irradiance and average cosine for diffuse irradiance in the vicinity of Cloud 1 at 400 nm in Elterman's standard atmosphere. Points lie on the surface along a line through the center of the shadow and perpendicular to the vertical plane containing the sun, cloud, and shadow center.

Fig. 10: Normalized downward diffuse irradiance and average cosine at shadow center and neighbor regions for Cloud 1 and Cloud 2 embedded in Elterman's standard atmosphere. Clear sky values represent conditions with no cloud present.

Fig. 11: Same as Figure 10, except Elterman's aerosol scaled so that $\tau_a(550\text{ nm}) = .0375$.

Fig. 12: Values of RHS of Eq. (18) for Cloud 1 and Cloud 2 embedded in Elterman's standard and scaled atmospheres.

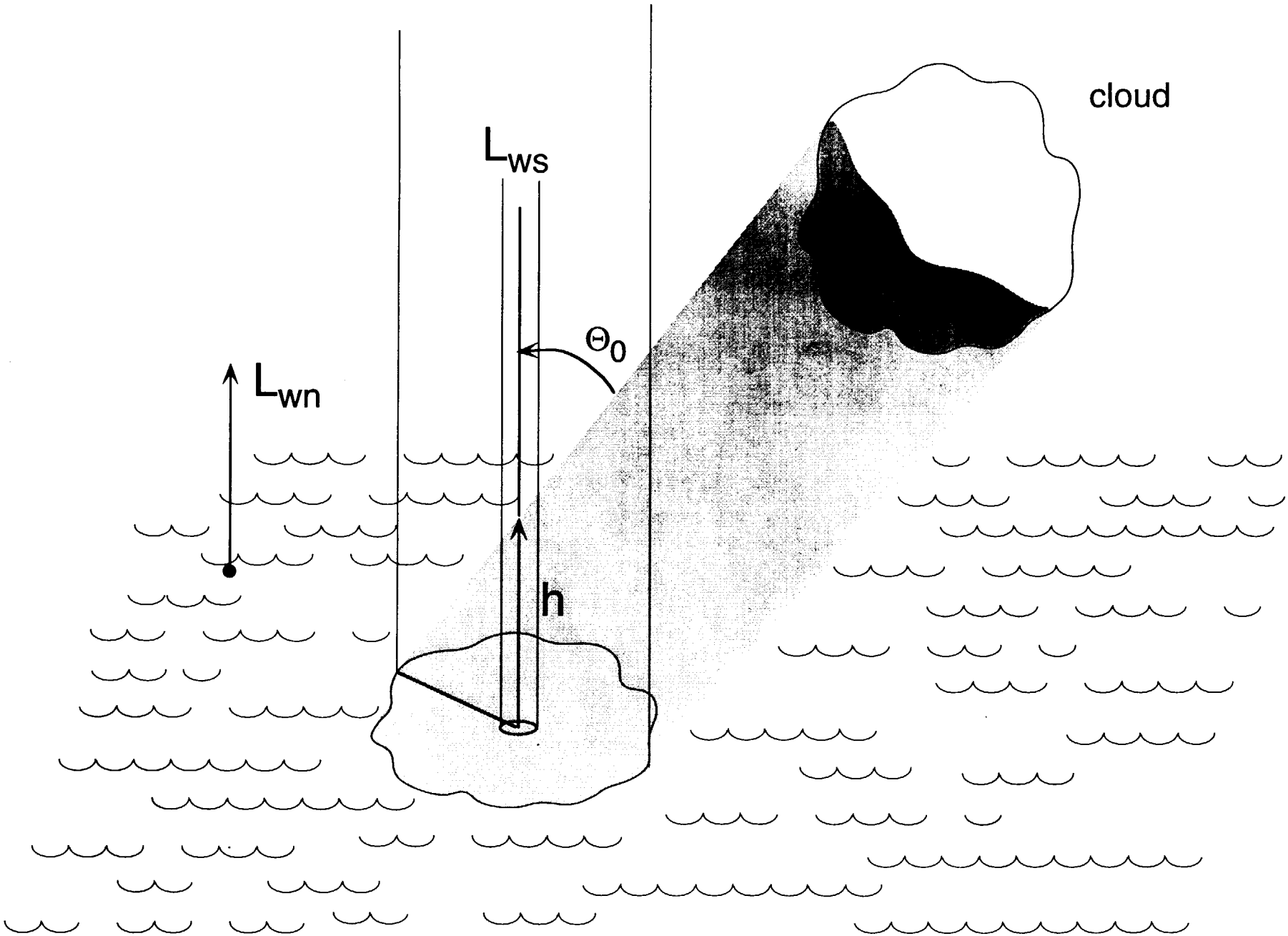
cloud
L_{ws}
Θ_0
L_{wn}
h

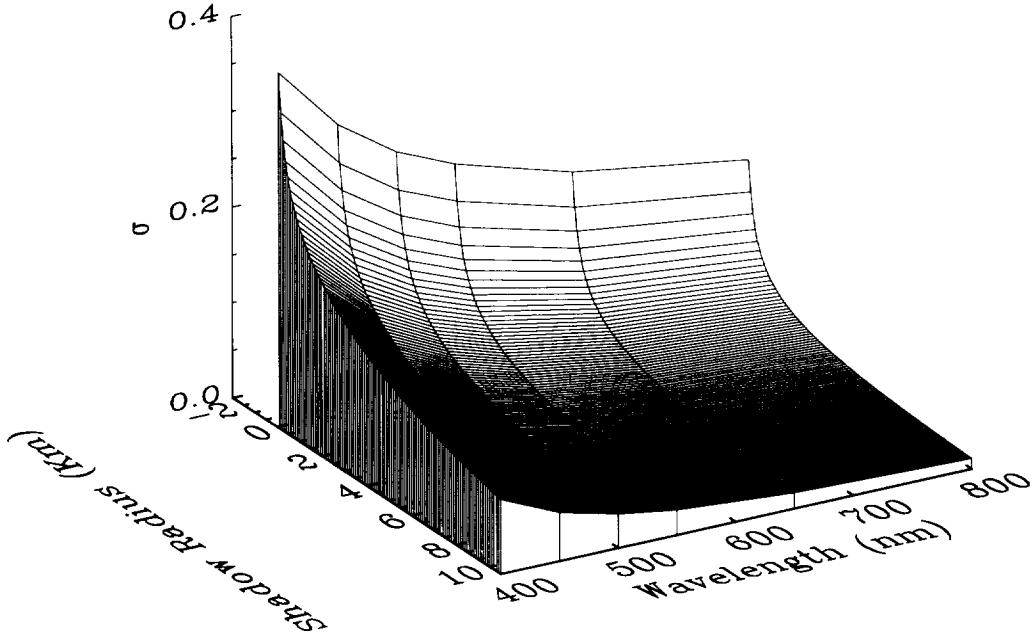

Figure 2. $\sigma(r,\lambda)$, from backward Monte Carlo simulation.

P. Reinersman, Applied Optics, Lasers, Photonics, and Environmental Optics.

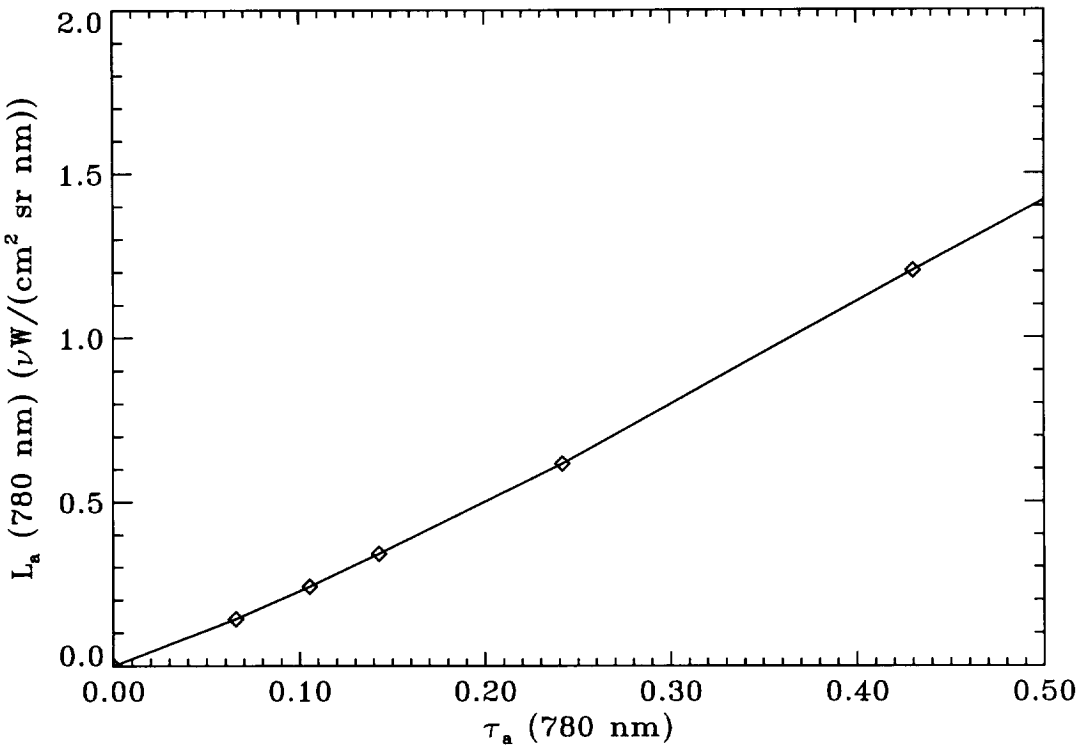

Figure 3. A scaling relationship between L_a(780 nm) and τ_a(780 nm) derived from LOWTRAN-7.

P. Reinersman, Applied Optics, Lasers, Photonics, and Environmental Optics.

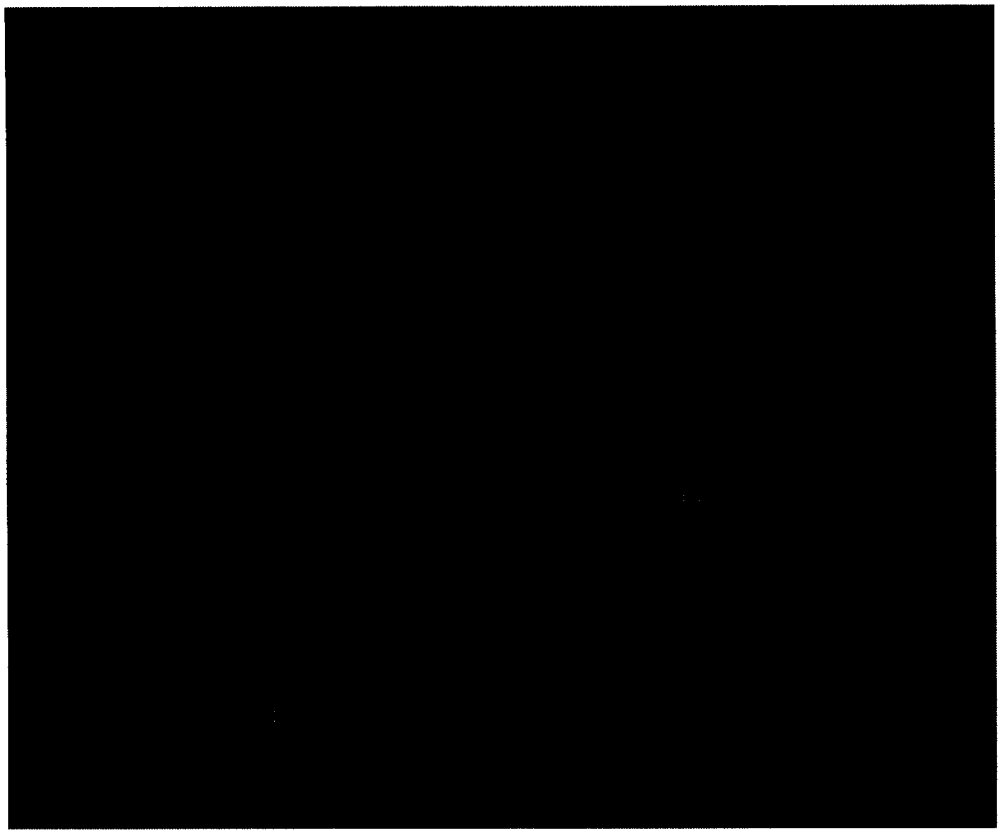

Figure 4. : The locations of sites where cloud-shadow method was used. Shadow and neighbor regions are marked by boxes.

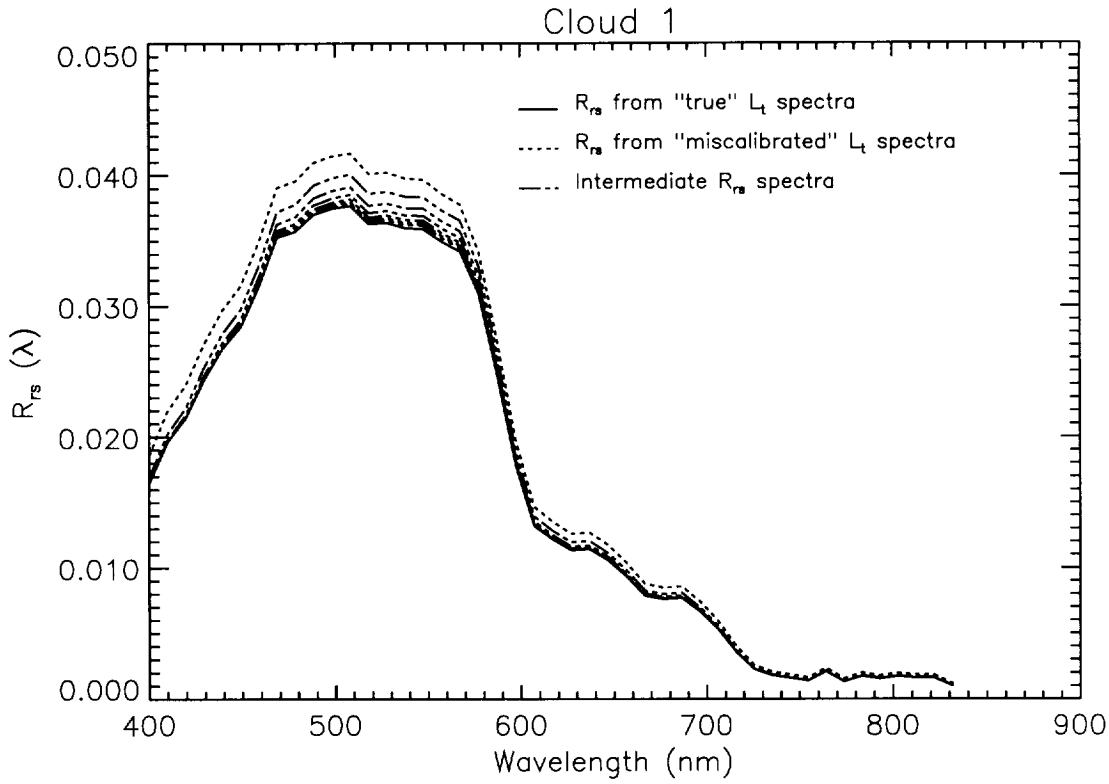

Figure 5. Illustration of the convergence of the cloud-shadow calibration. Solid line is "true" R_{rs}, dotted line is R'_{rs} which would be derived if sensor calibration had been in error by 10%. Intermediate lines indicated the iterative convergence of the cloud-shadow method.

P. Reinersman, Applied Optics, Lasers, Photonics, and Environmental Optics.

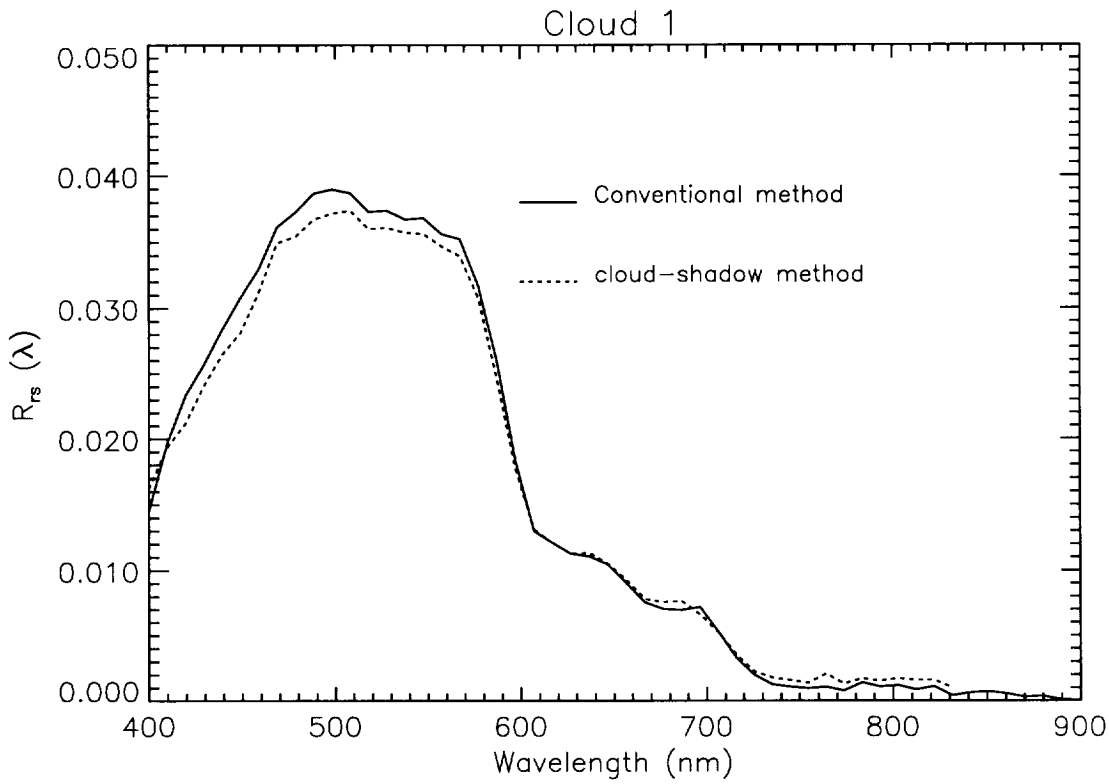

Figure 6. Remote-sensing reflectance spectra from the bottom site neighborhood of Figure 2 using conventional atmospheric-correction methods and the cloud-shadow method.

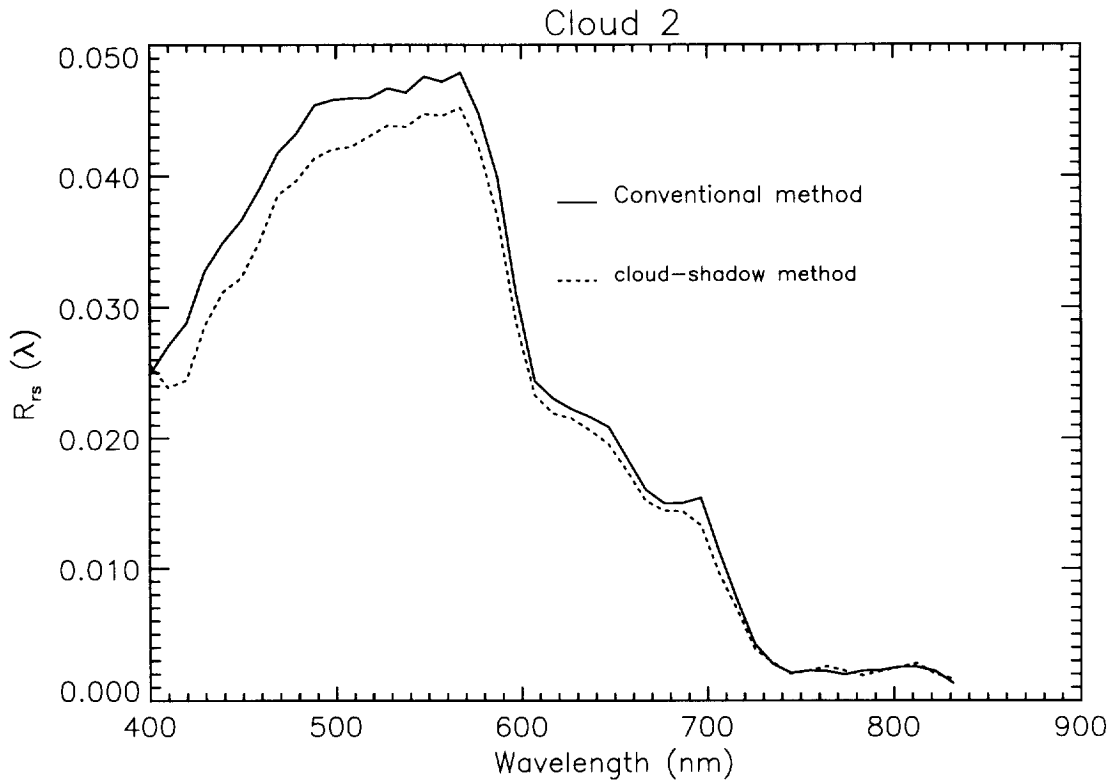

Figure 7. Remote-sensing reflectance spectra from the top site neighborhood of Figure 2 using conventional atmospheric-correction methods and the cloud-shadow method.

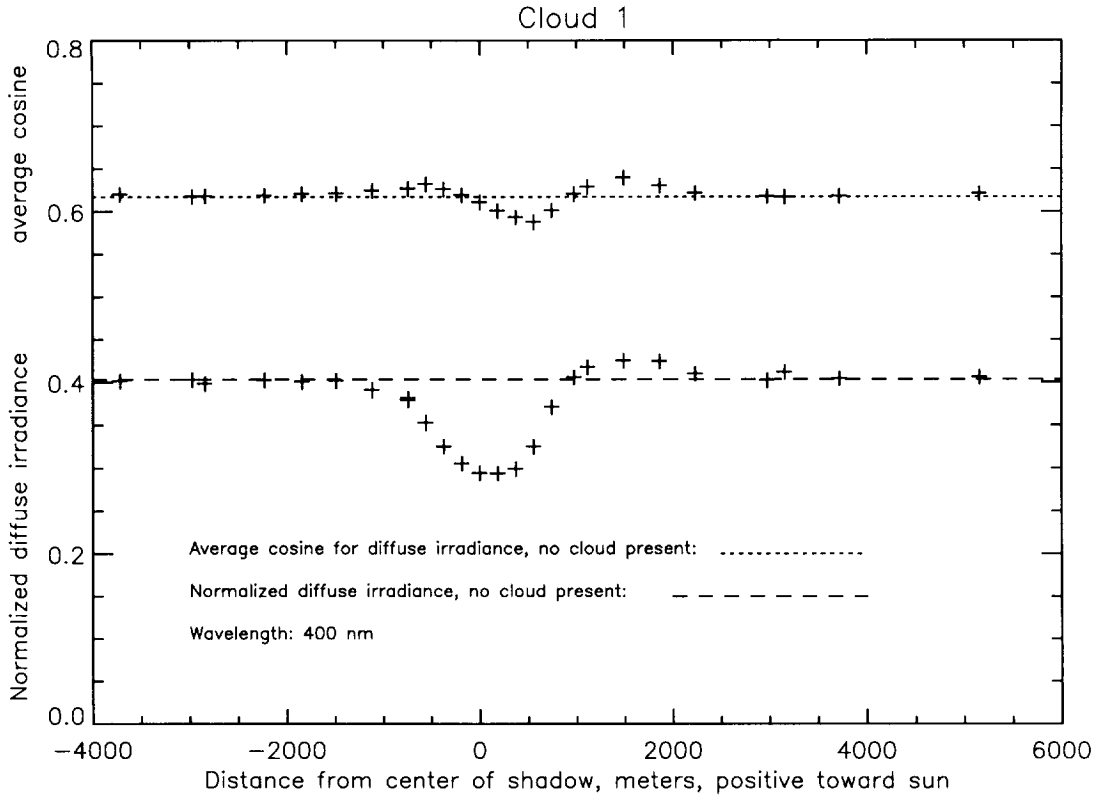

Figure 8. Normalized downward diffuse irradiance and average cosine for diffuse irradiance in the vicinity of Cloud 1 at 400 nm in Elterman's standard atmosphere. Points lie on the surface in the vertical plane containing the sun, cloud, and shadow center.

P. Reinersman, Applied Optics, Lasers, Photonics, and Environmental Optics.

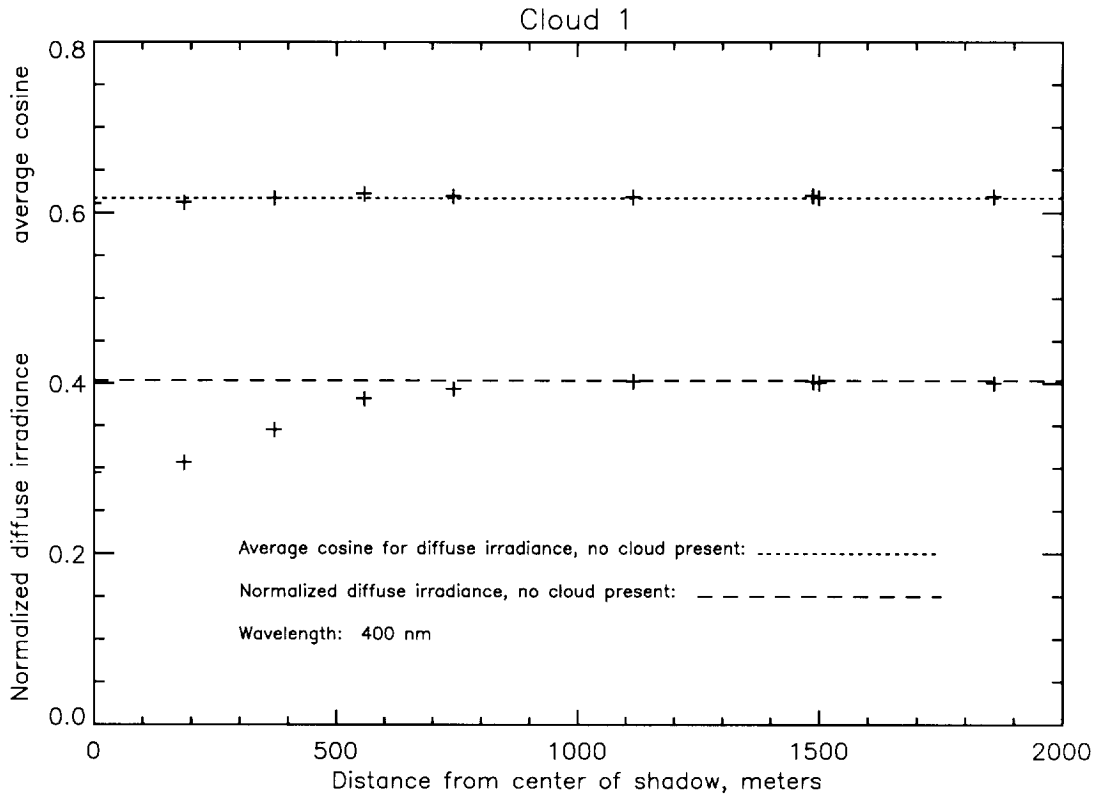

Figure 9. Normalized downward diffuse irradiance and average cosine for diffuse irradiance in the vicinity of Cloud 1 at 400 nm in Elterman's standard atmosphere. Points lie on the surface along a line through the center of the shadow and perpendicular to the vertical plane containing the sun, cloud, and shadow center.

P. Reinersman, Applied Optics, Lasers, Photonics, and Environmental Optics.

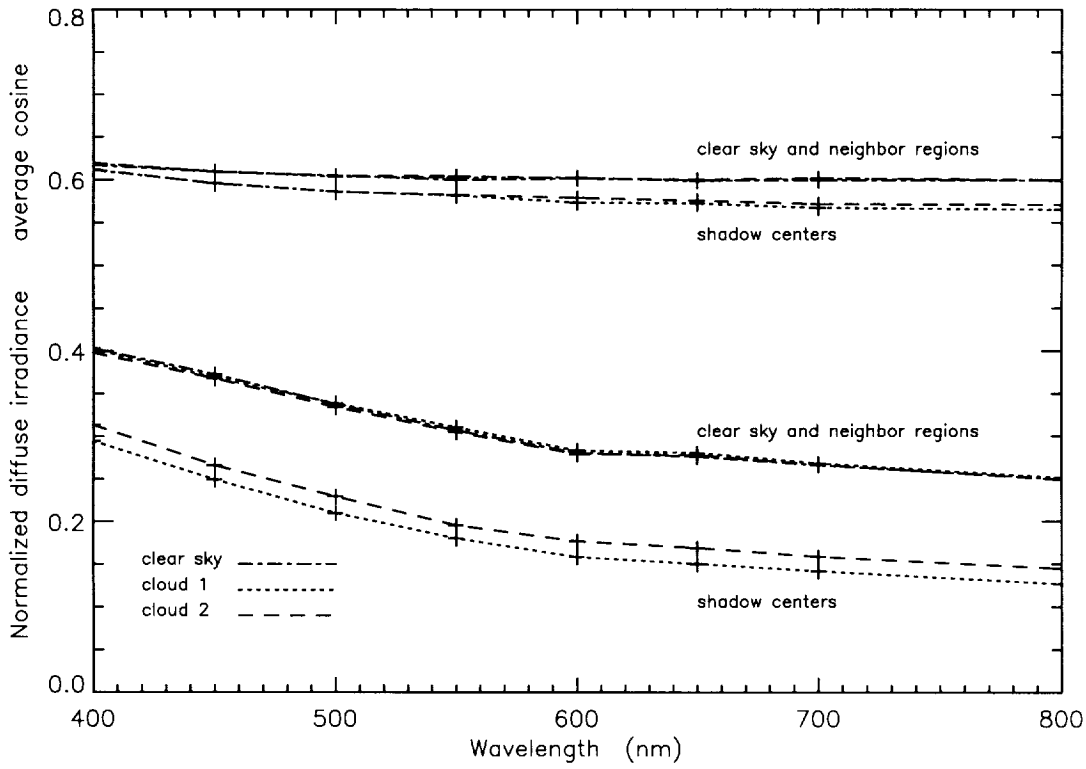

Figure 10. Normalized downward diffuse irradiance and average cosine at shadow center and neighbor regions for Cloud 1 and Cloud 2 embedded in Elterman's standard atmosphere. Clear sky values represent conditions with no cloud present.

P. Reinersman, Applied Optics, Lasers, Photonics, and Environmental Optics.

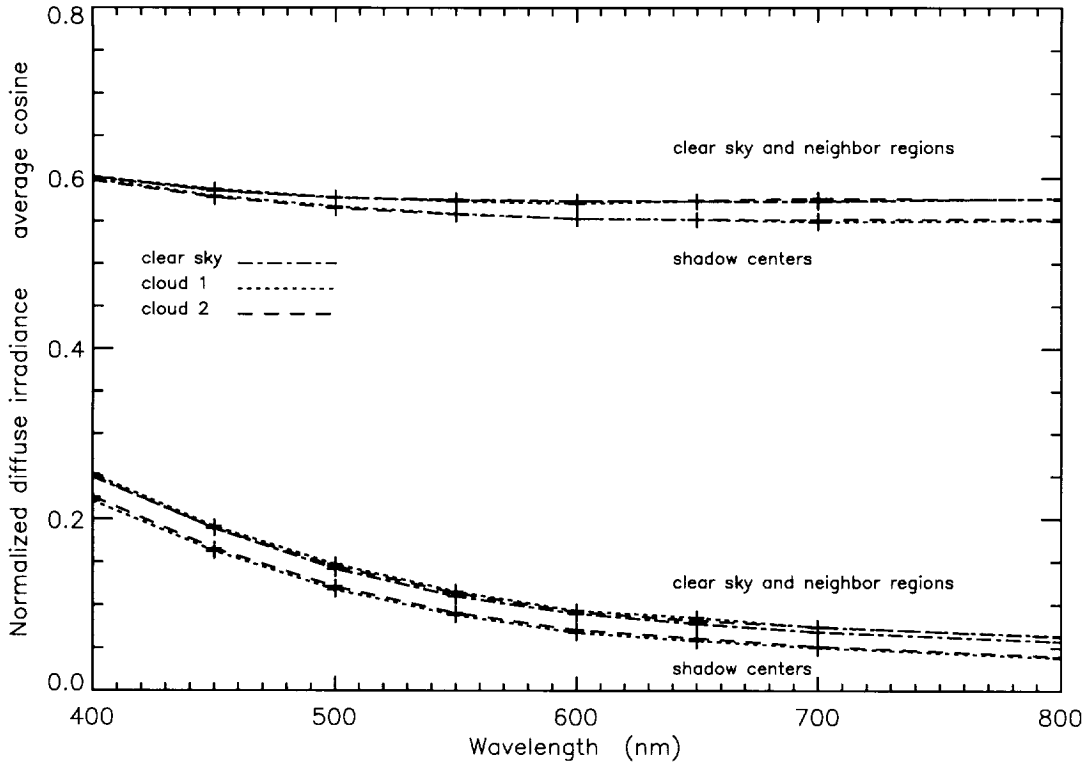

Figure 11. Same as Figure 10, except Elterman's aerosol scaled so that $\tau_a(550\text{ nm}) = .0375$.

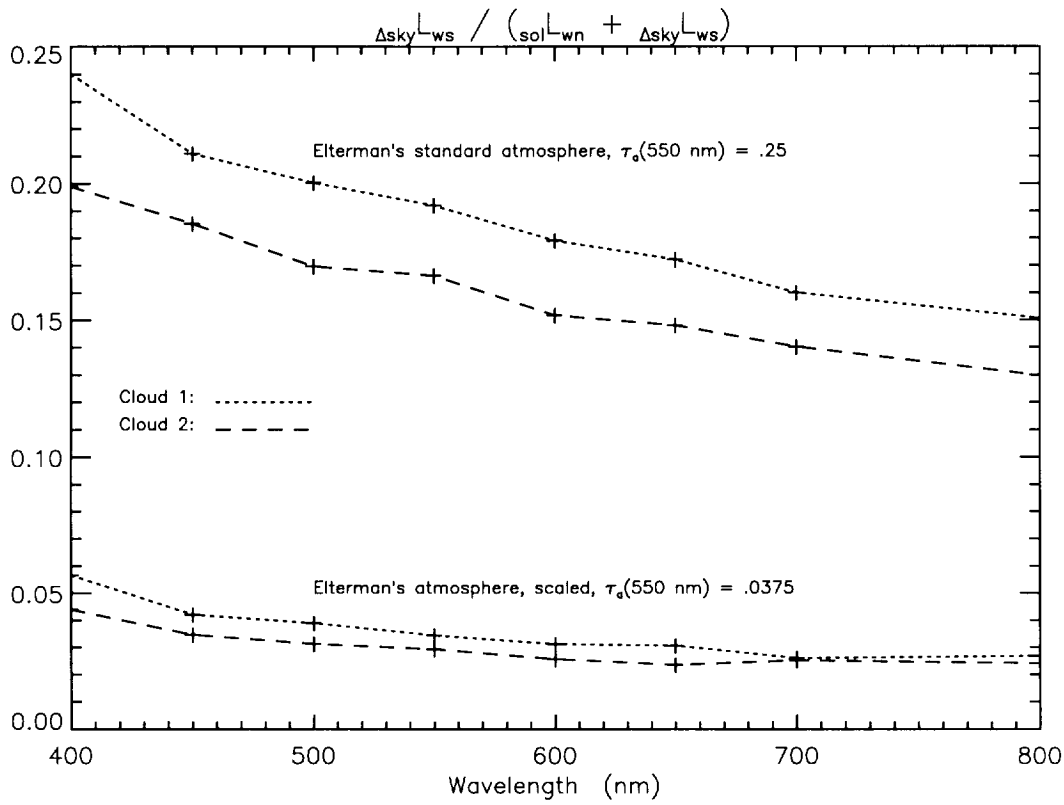

Figure 12. Values of RHS of Eq. (18) for Cloud 1 and Cloud 2 embedded in Elterman's standard and scaled atmospheres.